Global atmospheric hydrogen chemistry and long-term source-sink budget simulation with the EMAC v2.55 model

Nic Surawski[1,2], Benedikt Steil[2], Christoph Brühl[2], Sergey Gromov[2], Klaus Klingmüller[2], Anna Martin[2], Andrea Pozzer[2,3], and Jos Lelieveld[2,3]

[1]Centre for Green Technology, University of Technology Sydney, Gadigal Country, NSW 2007, Australia
[2]Atmospheric Chemistry Department, Max Planck Institute for Chemistry, 55128 Mainz, Germany
[3]Climate and Atmosphere Research Center, The Cyprus Institute, Nicosia, Cyprus

Correspondence: Nic Surawski (Nicholas.Surawski@uts.edu.au)

Abstract

In this study, we use an earth system model with detailed atmospheric chemistry (EMAC v2.55.2) to undertake simulations of hydrogen (H_2) atmospheric dynamics. Long-term simulations were performed globally with a horizontal resolution of 1.9 degrees with results being compared with observational data from 56 stations in the National Oceanic and Atmospheric Administration (NOAA) Global Monitoring Laboratory (GML) Carbon Cycle Cooperative Global Air Sampling Network.
5 We introduced H_2 sources and sinks, the latter through a soil uptake scheme, that accounts for bacterial consumption. The model thus accounts for detailed H_2 and methane (CH_4) flux boundary conditions. Results from the EMAC model are accurate and predict the magnitude, amplitude and interhemispheric seasonality of the annual hydrogen cycle at most observational stations. Time series comparison of EMAC and observational data produces Pearson correlation coefficients in excess of 0.9
10 at eight stations that experience well-mixed air masses free from direct anthropogenic perturbation. A further 23 stations yielded correlation coefficients between 0.7–0.9 in remote tropical or mid-latitude locations. The quality of model predictions is reduced in anthropogenically highly polluted stations in east Asia and the Mediterranean region and stations impacted by peat fire emissions in Indonesia, as local and incidental emissions are difficult to capture. Our H_2 budget corroborates bottom-up estimates in the literature in terms of source and sink strengths and overall atmospheric burden. By realistically simulating
15 hydroxyl radicals in the atmosphere, we show that the EMAC model is a capable tool for undertaking high accuracy simulation of H_2 at global scale. Future research applications could target the impact of potentially significant natural and anthropogenic H_2 sources on air quality and climate, reducing uncertainties in the H_2 soil sink and impacts of H_2 release on the future oxidising capacity of the atmosphere.

1 Introduction

Hydrogen represents an essential energy vector for 2050 net zero decarbonisation targets to be met. Current demand for hydrogen equates to approximately 95 Mt per year with existing uses in the refining industry, as well as the chemical industry for production of ammonia, methanol and other chemicals (Hydrogen Council, 2021; International Energy Agency, 2023). Hydrogen is also used in the direct reduction of iron along with smaller uses in electronics, glassmaking and metal processing (International Energy Agency, 2023). With increased governmental, financial and policy support, demand for hydrogen is forecasted to rise to between 430-690 Mt by 2050 (Hydrogen Council, 2021; International Energy Agency, 2023). Achieving this projected level of hydrogen demand can support clean energy use in: 1) hard to abate sectors such as long-haul trucking, shipping and aviation, 2) sectors that require a clean molecule as a chemical feedstock such as for co-firing of natural gas turbines or industrial processes such as steel manufacturing, 3) sectors that require a source of low carbon heat such as for cement and aluminium production or for buildings (Hydrogen Council, 2021; International Energy Agency, 2023). Use of hydrogen offers a lot of potential for securing decarbonisation outcomes, provided clean production pathways are prioritised (Hydrogen Council, 2021; International Energy Agency, 2023), carbon capture and storage technologies (if required) work efficiently and at scale (International Energy Agency, 2020),and leakage rates in the hydrogen value chain are minimised with sound engineering design (Esquivel-Elizondo et al., 2023; Fan et al., 2022).

Despite these potential advantages for decarbonisation, hydrogen has well-documented climate impacts following its release into the atmosphere which represents an important environmental challenge. In terms of climate impacts, hydrogen is an indirect greenhouse gas that leads to increases in 1) CH_4 lifetime due to hydrogen competing for the hydroxyl radical sink 2) tropospheric ozone production due to a chain of reactions initiated by the H atom and 3) stratospheric water vapour that enhances radiative forcing (Derwent et al., 2006; Paulot et al., 2021; Ocko and Hamburg, 2022; Warwick et al., 2022, 2023). Since hydrogen release affects the oxidising capacity of the atmosphere, it can also lead to changes in the production of sulphate, nitrate and secondary organic aerosols (Sand et al., 2023). Arising from these observations, coupled chemistry-climate modelling has a vital role to play before future hydrogen infrastructure is installed to ensure that projected increases in hydrogen utilisation do not lead to significant adverse consequences for the earth's atmosphere, air quality and climate.

Simulation of hydrogen atmospheric chemistry impacts has attracted significant research attention both in the past few decades (Hauglustaine and Ehhalt, 2002; Schultz et al., 2003; Tromp et al., 2003; Warwick et al., 2004) and at present (Derwent et al., 2020; Paulot et al., 2021, 2024; Warwick et al., 2023) given the likelihood that demand for hydrogen usage will grow and potential environmental impacts still require a solution. Previous attempts at simulating hydrogen mixing ratios with coupled chemistry-climate modelling have met variable levels of success at global scale. In this article, we show that the EMAC model is a highly capable tool for capturing 1) the magnitude, amplitude and seasonality of the annual H_2 cycle and 2) the meridional gradients in H_2 mixing ratios. We find that correctly representing the oxidising capacity of the atmosphere is critical for predicting H_2 mixing ratios and their spatio-temporal variability which is an outcome that the EMAC model supports.

2 Materials and methods

In this work, we employ the EMAC model which couples the 5th generation European Centre Hamburg General Circulation Model (ECHAM5; Roeckner et al. (2003, 2004, 2006)) to the Modular Earth Submodel System (MESSy) (Jöckel et al., 2006, 2010). Simulations were performed with T63 spectral resolution which produces a spatial resolution of 1.9 ° (approximately 180–190 km). Simulations were performed with 90 levels up to 80 km above the earth's surface, encompassing both the lower and middle atmosphere. Chemical reactions in the atmosphere were modelled with version 1 of the Mainz Isoprene Mechanism (MIM1; Pöschl et al. (2000); Jöckel et al. (2006)). The model experiment covers the time period 2006-2023, with the first three years used as spin-up time. Flux boundary conditions were employed for both CH_4 and H_2 to overcome issues with the introduction of artificial sources and sinks arising from using Dirichlet boundary conditions with a prescribed mixing ratio at the lower boundary of the atmosphere. To reach a steady-state for the control simulation, the initial conditions for CH_4 and H_2 were obtained from a 15 years long simulation, covering the period 1990-2005. Methane was simulated based on the work of Zimmermann et al. (2020), in which emissions of CH_4 and deposition are represented based on the year 2020. Integration of the equations in the simulation uses a time-step of 450 seconds, and, due to the relatively long lifetime of H_2, precluding diel variability, instantaneous values are outputted every day.

2.1 Emissions

In this work, the goal is to undertake an equilibrium simulation that reaches steady-state mixing ratios representative of present day atmospheric conditions. Therefore, emissions are based on the year 2020 and are repeated for each year, removing any interannual variability.

For the long-lived tracer CH_4, the a-posteriori emissions estimated by Zimmermann et al. (2020) for the year 2020 have been used, which have been shown to be efficient for simulating interactive CH_4 in the EMAC model. Twelve emission categories are considered here, namely, swamps or wetlands (SWA), animals (ANI), landfills (LAN), rice paddies (RIC), gas production (GAS), shale gas drilling (SHA), bogs (BOG), coal mining (COA), including minor natural sources from oceans, other anthropogenic sources, volcanoes, oil production and offshore traffic, oil-related emissions (OIL), biomass burning (BIB), termites (TER), and biofuel combustion (BFC). Only emissions from bogs, rice fields, swamps, and biomass burning are subject to seasonal variability. Most of the emissions are based on the emission fields of the Global Atmospheric Methane Synthesis (GAMeS) in which processes with similar isotopic characteristics are aggregated into one group (Houweling et al., 1999). For biomass burning, the GAMeS dataset is replaced by the GFEDv4s (Randerson et al., 2017) and is vertically distributed according to a profile suggested in the EDGAR database (Van Aardenne et al., 2005). The GFEDv4s biomass burning statistics include agricultural waste burning events. A total amount of 601.1 Tg yr^{-1} of CH_4 is emitted in the model and detailed emissions for each sector can be found in Table 1 and 3 of Zimmermann et al. (2020), which also describe in detail the emission optimisation process.

H_2 emissions were taken from the RETRO dataset (Schultz et al., 2008), which was chosen due to its completeness. As for the other sources we repeated the emissions based on one single year, namely the year 2000. The RETRO database covers the

period 1960-2000, and the last year was taken as representative of 2020 emissions, motivated by the stagnation of H_2 emissions in the past few decades (Paulot et al., 2021). A global value of 14.3 Tg yr^{-1} for anthropogenic emissions is obtained from the RETRO database, as well as 4.8 Tg yr^{-1} from soil emissions. Biomass burning emissions were obtained from the GFED (Global Fire Emissions Database) database (Giglio et al., 2013), and accounted for 8.35 Tg yr^{-1}. As the RETRO oceanic emissions are outside the range of emissions suggested by the literature (Paulot et al., 2024), these emissions were upscaled to 3 Tg yr^{-1} so to be within the suggested range (i.e. between $3-6$ Tg yr^{-1}).

For non-GHGs, different emissions were adopted. Anthropogenic sources of short-lived gases are based on CAMS-GLOB-ANTv4.2 and CAMS-GLOB-AIRv1.1 (Granier et al., 2019), and the emissions are estimated without reduction due to lockdowns during the COVID-19 pandemic (Reifenberg et al., 2022). Biomass burning emissions are calculated online on a daily basis and rely on dry matter burned from observations and fire type (Kaiser et al., 2012). The emission factors for different tracers and fire types are taken from Andreae (2019) and Akagi et al. (2011). The ONEMIS submodel (Kerkweg et al., 2006) calculates natural emission fluxes of sea salt (Guelle et al., 2001) and dust (Klingmüller et al., 2018; Astitha et al., 2012). The biogenic emissions of organic species have been compiled following Guenther et al. (1995) and are prescribed in the model in an offline manner (Kerkweg et al., 2006), with the exception of biogenic isoprene and terpenes, for which the emissions are calculated online (Kerkweg et al., 2006).

2.2 Soil sink implementation

We estimate the soil sink using a two-layer soil model (Yonemura et al., 2000; Ehhalt and Rohrer, 2013a; Paulot et al., 2021). Hydrogen is assumed to diffuse through a dry top layer of soil with no bacterial activity (layer I), which may be covered by an equally inactive layer of snow. In a second layer below the top layer (layer II), the rate of H_2 removal by high-affinity hydrogen-oxidising bacteria (Paulot et al., 2021) depends on both soil temperature and moisture. The resulting deposition rate is parameterised by:

$$v_{\mathrm{d}} = \frac{1}{\left(\delta/D_{\mathrm{soil}}(\theta_{\mathrm{w,I}}) + \delta_{\mathrm{snow}}/D_{\mathrm{snow}} + 1/\sqrt{(D_{\mathrm{soil}}(\theta_{\mathrm{w,II}})\ A\ g(T)\ f(\theta_{\mathrm{w,II}}/\theta_{\mathrm{p}}))} \right)}\ . \tag{1}$$

The first two terms in parenthesis in the denominator of Eq. (1) represent diffusion through the inactive soil layer and the snow layer of thickness δ and δ_{snow}, respectively. The diffusivity of H_2 in soil is given by Millington and Quirk (1959):

$$D_{\mathrm{soil}}(\theta_{\mathrm{w}}) = ((\theta_{\mathrm{p}} - \theta_{\mathrm{w}})^{3.1}/\theta_{\mathrm{p}}^2)D_{\mathrm{air}}, \tag{2}$$

which depends on the volumetric soil water fraction θ_{w} and the volumetric soil pore fraction (i.e. porosity) θ_{p}. The diffusivity of H_2 in snow is given by:

$$D_{\mathrm{snow}} = 0.64\ D_{\mathrm{air}}, \tag{3}$$

while the diffusivity of H_2 in air is given by:

$$D_{\text{air}} = 0.611 \, \frac{((T+273.15)/273.15)^{1.75}}{p/1013.25}, \tag{4}$$

where the diffusivity of H_2 in air depends on the air temperature T in $^\circ$C and the air pressure p in hPa.

The third term in parenthesis in the denominator of Eq. (1) represents H_2 removal in the lower, active layer. The temperature dependence is given by Ehhalt and Rohrer (2011):

$$g(T) = \frac{1}{(1+\exp(-(T-3.8)/6.7)} + \frac{1}{(1+\exp((T-62.2)/7.1)} - 1, \tag{5}$$

where T is the soil temperature in $^\circ$C.

The soil moisture dependence in terms of the water saturation $S = \theta_{\text{w}}/\theta_{\text{p}}$ for eolian sand is given by Ehhalt and Rohrer (2011):

$$f_{\text{es}}(S) = 0.00936 \frac{(S - S_{\text{es}}^*)(1-S)}{S^2 - 0.1715S + 0.03144}, \tag{6}$$

where $S_{\text{es}}^* = 0.02640$ is the minimum level of water saturation required for microbial activity. For loess loam the soil moisture dependency is given by Ehhalt and Rohrer (2011):

$$f_{\text{ll}}(S) = 0.01997 \frac{(S - S_{\text{ll}}^*)(0.8508-S)}{S^2 - 0.7541S + 0.2806}, \tag{7}$$

where $S_{\text{ll}}^* = 0.05369$. For a mixture of eolian sand and loess loam we use the weighted mean given by:

$$f(S) = \varphi_{\text{sand}} f_{\text{es}}(S) + (1 - \varphi_{\text{sand}}) f_{\text{ll}}(S), \tag{8}$$

where φ_{sand} is the sand fraction of the soil.

The constant A represents bacterial activity and is adjusted to obtain a global mean deposition velocity of 0.033 cm s^{-1} over land during 2012 to 2015 (Yashiro et al., 2011).

The thickness of the upper soil layer without hydrogenase (i.e. an enzyme in prokaryotes such as bacteria that consume H_2) activity is parametrised by:

$$\delta_{\text{s}} = 0.0057((\theta_{\text{p}} - \theta_{\text{w}})/\theta_{\text{w}})^{2.5}, \tag{9}$$

in sandy loam and

$$\delta_{\text{l}} = 0.109((\theta_{\text{p}} - \theta_{\text{w}})/\theta_{\text{w}})^{1.8}, \tag{10}$$

in loam. Both δ_{s} and δ_{l} are expressed in cm. For a mixture of sandy loam and loam with sand fraction φ_{sand} we use the weighted mean to calculate the soil layer thickness via:

$$\delta = \varphi_{\text{sand}} \delta_{\text{s}} + (1 - \varphi_{\text{sand}}) \delta_{\text{l}}. \tag{11}$$

The soil water content in the top, dry layer (i.e. θ_{wI}) is assumed to be the threshold moisture content below which the bacterial activity vanishes and is given by:

$$\theta_{\mathrm{wI}} = S^* \theta_{\mathrm{p}}, \tag{12}$$

where $S^* = S_{\mathrm{es}}^*$ is the threshold moisture content for eolian sand and $S^* = S_{\mathrm{ll}}^*$ for loess loam.

Accordingly, the remaining water within the top 10 cm of soil is between depth δ and 10 cm, resulting in a soil water content for the second layer (i.e. θ_{wII}) of:

$$\theta_{\mathrm{wII}} = \frac{10\theta_{\mathrm{w}} - \delta\theta_{\mathrm{wI}}}{10 - \delta}. \tag{13}$$

We evaluated Eq. (1) using monthly reanalysis data for soil moisture, soil temperature, air pressure, snow depth and snow density with $0.25°$ grid spacing from the ERA5 dataset provided by the European Centre for Medium-Range Weather Forecasts (ECMWF) (Hersbach et al., 2020, 2023). The mean soil moisture and soil temperature for the top 10 cm soil layer was obtained by linearly interpolating the ERA5 soil level data. The volumetric soil water content was then uniformly reduced by 6 % (Paulot et al., 2021). Static soil porosity and sand fraction maps with $0.25°$ grid spacing were obtained from the Land Data Assimilation System (LDAS) (Rodell et al., 2004; GLDAS, 2024).

2.3 Observations

EMAC simulations are compared with observational data from 56 stations (with more than 12 monthly values) that form part of the NOAA GML Carbon Cycle Cooperative Global Air Sampling Network (Petron et al., 2024). Data gaps exist at some stations due to the application of quality control procedures, as well as missing data due to impacts of the COVID-19 pandemic. For comparison with the results of the EMAC equilibrium simulation, the observed monthly values have been detrended by subtracting the trend obtained by a sixth order harmonic regression with a linear trend term, while keeping the mid-year values for 2020 fixed.

3 Results

Figure 1 presents a global map of modelled annual mean H_2 mixing ratios as well as the location of observational stations that we use for model inter-comparison purposes. This global map shows the inter-hemispheric gradient for this molecule whereby H_2 mixing ratios are higher in the southern hemisphere compared to the northern hemisphere. This global map also shows the influence of pollution hotspots in Asia, and the influence of biomass burning emissions in central Africa and peat fire emissions in southeast Asia.

We show time series data for model comparisons with observational data (without gaps in monthly data) from 20 observational stations in Fig. 2. Further comparisons with observational data from another 36 observational stations (with data gaps) are shown in Fig. B1 and B2. Across these 56 observational stations, the Pearson correlation coefficient (r) exceeds 0.9 for eight stations that are free from direct anthropogenic perturbation. Such stations are either remote or located at high latitude
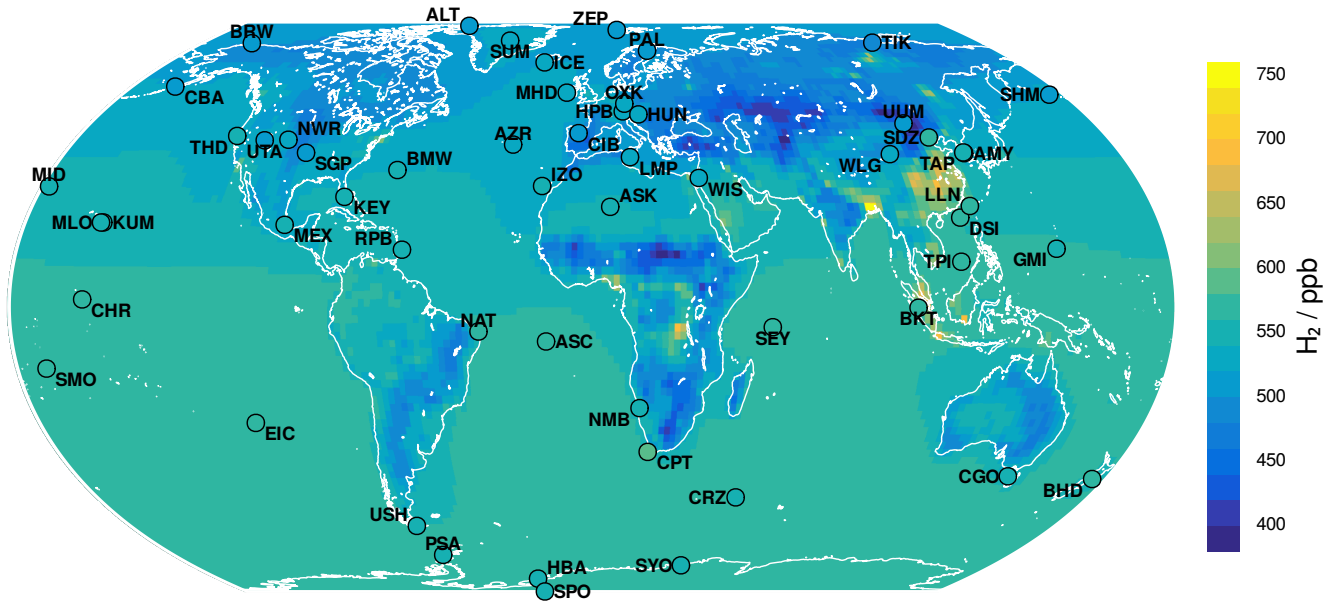
Figure 1. Global map of H$_2$ mixing ratios and the location of observational stations. Model data is averaged over the years 2010–2023 (inclusive) which is representative of the year 2020 for a steady-state simulation, while observational data uses mid-2020 values from a detrending fit using a sixth order harmonic regression technique.

in either the Arctic or Antarctic regions. In such cases, the annual cycle of H$_2$ is modelled excellently in terms of magnitude,
amplitude and seasonality. In contrast, the three stations in the Mediterranean region; namely, Lampedusa (LMP, 0.04), CIBA
in northern central Spain (CIB, -0.17) and Israel (WIS, -0.29) produce correlation coefficients close to zero or even negative.
The same holds for two stations located in Shangdianzi (China, SDZ, -0.2) and Ulaan Uul (Mongolia, UUM, 0.03). The EMAC
model is under-performing at two tropical coastal stations, Natal (Brazil, NAT) and Bukit (Indonesia, BKT) with correlation
coefficients of 0.14 in contrast to other tropical stations. These stations are located in regions that are strongly influenced by di-
rect anthropogenic emissions (e.g. Mediterranean region, UUM, SDZ) or are impacted by biomass burning (i.e. NAT) and peat
fire emissions (i.e. BKT). Negative r values suggest that the EMAC model does not correctly capture the phasing of the annual
H$_2$ cycle which results in an anti-correlation in Table B1. Another 23 stations have correlation coefficients between 0.7–0.9
which demonstrate very good agreement between model and observational data. A number of these stations are located in the
mid-latitudes either in the northern or southern hemisphere. The remaining 18 stations produce correlation coefficients between
0.3–0.7 mostly in either remote tropical or mid-latitude regions. Overall, the results are very promising and demonstrate the
ability of the EMAC model to predict H$_2$ mixing ratios accurately in most regions of the earth. To provide a visual overview
of these results, Fig. 3 provides a global map of Pearson correlation coefficients for comparison of EMAC and observational
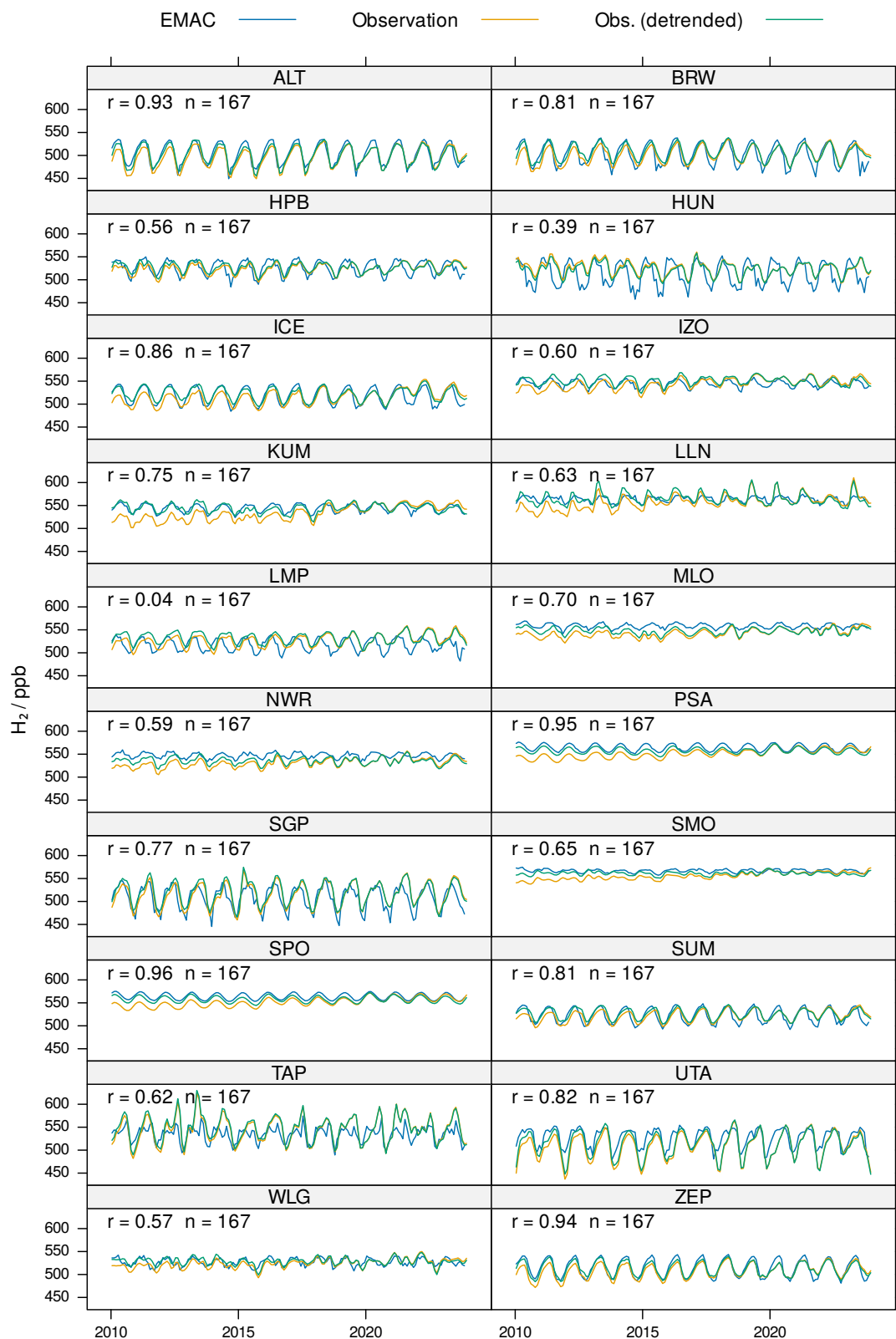data.

Figure 2. Time series comparison of observational and EMAC model data for H_2. Results are presented for 20 stations without any gap in monthly data. The sample size for observational data is denoted by n, while r is the Pearson correlation coefficient.
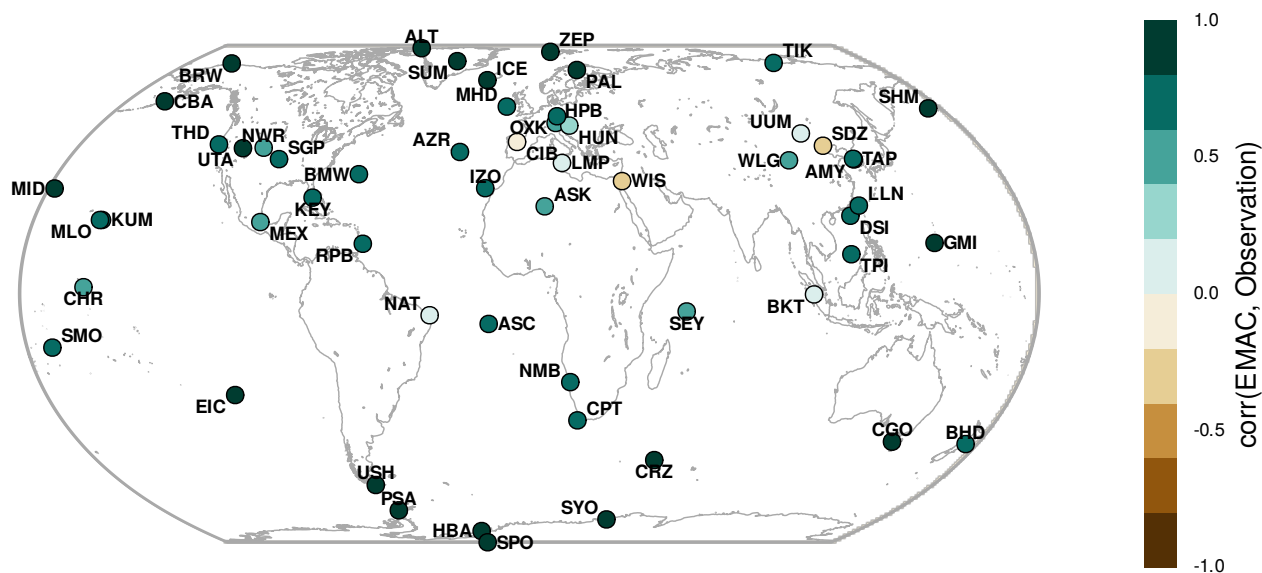
Figure 3. Pearson correlation coefficient for the intercomparison between EMAC and observational data for H_2. Model data is compared with detrended observational data for the years 2010–2023 (inclusive) to perform this calculation.

We also present a plot of the meridional gradient in H_2 in Fig. 4. Overall, meridional gradients in H_2 are captured very well

185   by the EMAC model, notably for stations located in the southern hemisphere, likely because many represent the background atmosphere, whereas many stations in the northern hemisphere are affected by local influences. The model correctly predicts higher H_2 mixing ratios in the southern hemisphere even though the majority of H_2 sources are present in the northern hemisphere. The predicted interhemispheric gradient in H_2 presented here is correct by virtue of the greater soil sink that is present in the northern hemisphere arising from its larger land area (Ehhalt and Rohrer, 2009). Most of the discrepancies between the

190   observed and predicted H_2 mixing ratios exist for a small number of stations within the northern hemisphere mid-latitudes (between 30-60 ° N) and in the tropics, presumably influenced by local source variability that is insufficiently resolved by our global model.

For further results, we refer the reader to Appendix B which provides further graphs and tabulated summaries of model performance.
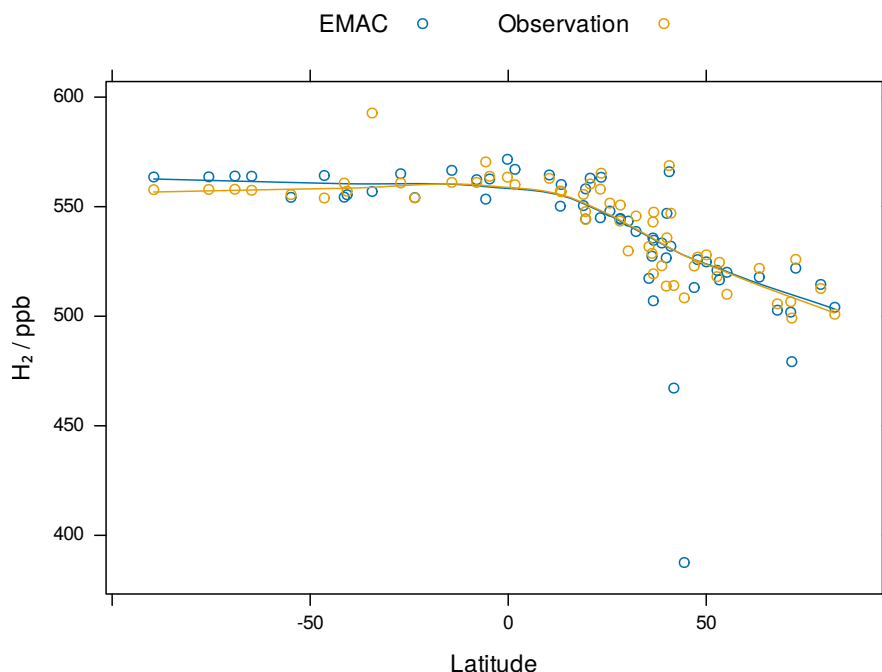
Figure 4. Meridional gradients in H_2 for EMAC predictions and observational data where stations had more than 12 monthly values. The solid lines were obtained by locally estimated scatterplot smoothing (LOESS; smoothing parameter 2 / 3, locally linear). Negative latitudes represent south and positive latitudes represent north of the equator. Data are shown for stations with more than 12 monthly values.

4   Discussion

4.1   Model comparison with observational data

A key feature of the results (Fig. 2, Fig. B1 and Fig. B2) is the ability of the EMAC model to realistically predict the magnitude, amplitude and seasonality of the annual H_2 cycle at most stations, in unison with that of CH_4 Zimmermann et al. (2020), with both compounds being modelled with flux boundary conditions and interactive sinks. Promising results are obtained especially for stations that experience well-mixed air masses free from direct anthropogenic influence, for example, in mostly polar regions, which are particularly sensitive to atmospheric transport and chemistry dynamics. The EMAC model results are also quite promising in a range of mid-latitude stations both in the northern and southern hemisphere. In contrast, there are some regions of the globe (Fig. 3) where results are not as promising. For example, the EMAC model predictions are less accurate in the highly anthropogenically polluted Mediterranean region, near the Amazonian region which is impacted by biomass burning emissions, and southeast Asia which is impacted by peat fire emissions. Due to the coarse spatial resolution of 180–190 km and limited information about local and incidental sources, the variability of mixing ratios in these regions is more challenging to capture. This is especially the case for some coastal stations (e.g. NAT, BKT) where the model is limited due to resolution in accurately representing the mixing of marine and continental air. Also the deviations in China and Mongolia (SDZ, UUM)

10

can be partly attributed to a resolution effect. Both stations are located close to strong horizontal gradients in H_2 mixing ratios.
The vertical resolution of the lowermost model layers (i.e. thicknesses of 66 m, 166 m, 319 m from the surface upwards) and the representation of the orography influence the comparison. It is important to consider the measurement height relative to the surface and the geographic prominence of the stations. For example, the modelled amplitude of the annual H_2 cycle can be reduced by up to 40% between the surface and the next model layer for continental stations due to the importance of the soil sink, whereas the H_2 mixing ratios increase with height driven by the strong atmospheric chemical H_2 production. In addition, an interesting model-measurement discrepancy occurs at the Weizmann Institute of Science (WIS) station near the northern Red Sea, where unaccounted for alkane emissions have been attributed to natural seepage from deep water sources (Bourtsoukidis et al., 2020), possibly accompanied by H_2 emissions. Overall, the EMAC model performs favourably at a global scale for simulating H_2 mixing ratios. Comparison with model output from Yashiro et al. (2011) shows that while the EMAC model produces correlation coefficients in excess of 0.7 for over half of the observational stations, the CHASER chemistry-climate model achieves the same result for only one quarter of all observational stations. The annual mean H_2 mixing ratios are well captured by the EMAC model (Table B1 and Fig. 4), with the exception of CIB (r=-0.17), UUM (r=0.03), and the coastal station Cape Town (CPT) despite its high Pearson correlation coefficient (r=0.73).

To successfully simulate H_2 mixing ratios in the atmosphere, a model needs to correctly resolve the complex interplay between meteorology and chemistry. In terms of chemistry, having the oxidising capacity of the atmosphere represented correctly is a key consideration (Prather and Zhu, 2024). Model intercomparisons performed by Nicely et al. (2020) suggests that many chemistry models underestimate CH_4 lifetime due to simulating an atmosphere that is overly enriched in OH radicals. Recently, work by Yang et al. (2024) concurs that several atmospheric chemistry models over-predict OH mixing ratios which has implications for CH_4 and H_2 lifetimes. Our estimate of the tropospheric chemical lifetime (Table 1) for CH_4 (i.e. 8.9 years) compares excellently with observational estimates of approximately 9.1 years (Holmes et al., 2013). For this reason, we believe that the EMAC model is realistically capturing the oxidising capacity of the atmospheric which helps to facilitate high-accuracy prediction of H_2 and CH_4 dynamics.

4.2 Budget and lifetimes

In the atmosphere, CH_4 and H_2 are tracers strongly connected with similar chemical fates. Table 1 shows that CH_4 and H_2 have nearly identical chemical lifetimes both in the troposphere and atmosphere. Furthermore the total sources of H_2 and CH_4, corrected for molecular masses, are very comparable. The biggest difference between these two compounds stems from hydrogen's much larger soil sink which reduces its tropospheric lifetime by approximately a factor of four compared to CH_4.

In Table 2, we compare our H_2 budget derived from EMAC model output with other estimates from the literature. We find that our H_2 budget agrees favourably with bottom-up literature estimates that rely on a combination of emission datasets and model calculations of turnovers and loss rates, but differs from top-down estimates relying on either inverse modelling (Xiao et al., 2007) or analysis of the ^2H (i.e. deuterium) budget (Rhee et al., 2006). Our overall budgeting of sources and sinks agrees very well with bottom-up estimates. In addition, our tropospheric H_2 lifetime is in very good agreement with bottom-up estimates. The tropospheric burden is in the upper range of model estimates. Note, that the upper boundary of the tropospheric

range is often not clearly defined in the literature, with different definitions e.g. 100 hPa, World Meteorological Organization (WMO), or a climatological tropopause being used. In this study the WMO tropopause definition is used based on a dynamic tropopause in high latitudes and lapse rate being used at low latitudes. The photochemical production is in between the range for bottom-up and top-down estimates (Paulot et al., 2021).These findings suggest that the EMAC model simulates a realistic atmospheric oxidation capacity which is a critical requirement for predicting H_2 mixing ratios well. Moreover, the small long-term trend in atmospheric H_2 captured by the model indicates the trend in global OH is also small, in turn relevant for the lifetime of CH_4 and other relatively long-lived trace gases.

Recent work by the United States Geological Survey (Ellis and Gelman, 2024) has developed a simple, zero-dimensional mass balance model coupled with Monte Carlo uncertainty analysis to explore global potential for geological (or gold) H_2 production in the earth's crust. Median modelled estimates of the subsurface H_2 resource are approximately 5.6×10^6 mega-tonnes. Ellis and Gelman (2024) estimate that global geological H_2 resources cause an additional global flux of 24 Tg yr^{-1} from the subsurface to the atmosphere. Interestingly, this potential unaccounted for source almost bridges the gap between bottom-up (55–60 Tg yr^{-1}) and top-down estimates (85–88 Tg yr^{-1}) for the dry deposition of H_2 (Paulot et al., 2021). Current knowledge concerning atmospheric H_2 mixing ratios does not exclude the existence of a large geological H_2 reservoir, and further emphasises the importance of dry deposition for the global atmospheric H_2 budget.

Table 1. Chemical budgets and lifetimes for H_2 and CH_4. Uncertainties are calculated as the standard deviation of multi-year annual means.

Budget term	H_2	CH_4
Tropospheric chemical sink (Tg yr^{-1})	19.0 ± 0.16	534.5 ± 4.04
Tropospheric chemical production (Tg yr^{-1})	49.5 ± 0.43	-
Tropospheric chemical lifetime (years)	8.7 ± 0.07	8.9 ± 0.07
Atmospheric chemical lifetime (year)	9.6 ± 0.07	9.8 ± 0.07
Soil sink (Tg yr^{-1})	60.5 ± 0.07	30.9 ± 0.02
Tropospheric lifetime (years)	2.1 ± 0.003	8.5 ± 0.06
Atmospheric lifetime (years)	2.5 ± 0.004	9.3 ± 0.06

4.3 Suggestions for future applications

Future research efforts in modelling H_2 atmospheric chemistry could build on the current work in three key ways. Firstly,
260   scenarios could be constructed to explore what role geological H_2 (i.e. gold H_2) holds for future atmospheric chemistry. If economically extractable reserves of gold H_2 are found, future utilisation of H_2 would increase well beyond current projections (Hand, 2023; Truche et al., 2024; Ellis and Gelman, 2024). It would therefore be critical to assess the atmospheric chemistry implications of vastly increased H_2 usage. Secondly, it will be critical to assess what impact H_2 use has on the future oxidising capacity of the atmosphere. Clean H_2 use will be associated with significant reductions in the co-emission of criteria pollutants
265   (Galimova et al., 2022) which will influence the formation of atmospheric oxidants such as ozone and hydroxyl radicals that constrain CH_4 and H_2 lifetimes (Archibald et al., 2011; Brasseur et al., 1998; Ganzeveld et al., 2010). Thirdly, the H_2 budget is dominated by the land sink (Tables 1 and 2) and future research efforts could help to constrain the important role played by a number of soil properties (e.g. porosity, soil moisture, temperature, and organic carbon content) on terrestrial H_2 uptake (Ehhalt and Rohrer, 2011, 2013a; Paulot et al., 2021; Smith-Downey et al., 2006). The production of H_2 by enzymes in soil
270   (i.e. hydrogenases) could also be considered in a depth-resolved manner as knowledge of the underlying processes improves (Ehhalt and Rohrer, 2013b). Recent coupling of the JSBACH vegetation model to EMAC by Martin et al. (2024) has developed a potential model tool for undertaking on-line H_2 land sink calculations.

Table 2. Tabulation of the H$_2$ budget from this study and from literature estimates. Uncertainties are calculated as the standard deviation of multi-year annual means.

Budget term	This study (EMAC)	Seiler and Conrad (1987)	Warneck (1988)	Novelli et al. (1999)	Hauglustaine and Ehhalt (2002)	Sanderson et al. (2003)	Rhee et al. (2006)	Price et al. (2007)	Xiao et al. (2007)	Ehhalt and Rohrer (2009)	Pieterse et al. (2011)	Yashiro et al. (2011)	Paulot et al. (2021)
Sources: Tg yr^{-1}													
Tropospheric	79.1 ± 0.4	87 ± 38	89	77 ± 16	70	78.2	107 ± 11	73		76 ± 14	77.3	73–80	74.4
Photochemical	49.5 ± 0.4	40 ± 15	50	40 ± 16	31	30.2	64 ± 12	34.3		41 ± 11	37.3	38–39	42.1
CH$_4$ oxidation	34.5 ± 0.4	15 ± 5	29	26 ± 9		15.2		24.5		23 ± 8			
VOC oxidation	15.0 ± 0.2	25 ± 10	21	14 ± 7		15		9.8		18 ± 7			
Direct	29.6	47	39	37	39	48	43	38.8	27	35	40	30–37	32.3
Ocean	3^a	4 ± 2	4	3 ± 2	5	4	6 ± 5	6 ± 3		6 ± 3	5	6	6
Biofuel								4.4					
Soil	4.8	3 ± 2	3	3 ± 1	5	4	6 ± 5	0		3 ± 2	3	3	3
Biomass burning	7.5	20 ± 10	15	16 ± 5	13	20	16 ± 3	10.1	12 ± 3	15 ± 6	15	8–15	9
Anthropogenic	14.3	20 ± 10	17	15 ± 10	16	20	15 ± 6	18.3	15 ± 10	11 ± 4	17	15.1–15.4	14.3
Atmospheric	81.1 ± 0.4								103 ± 10				
Photochemical	51.5 ± 0.4								76 ± 9				
Stratospheric CH$_4$ oxidation	1.94 ± 0.02												
Stratospheric VOC oxidation	0.08 ± 0.02												
Sinks: Tg yr^{-1}	81.2 ± 0.2	98 ± 23	89	75 ± 41	70	75.4	107 ± 11	73	103.9	79	77.9	75–78	75.1
Soil uptake	60.5^b ± 0.1	90 ± 20	78	56 ± 41	55	58.3	88 ± 11	55 ± 8.3	84 ± 8	60	55.8	57–60 ± 12	54.7
Photochemical	20.8 ± 0.2	8 ± 3	11	19 ± 5	15	17.1	19 ± 3	18	19.9	19	22.1	17–18	20.4
Troposphere	19.0 ± 0.2								18 ± 3				
Stratosphere	1.8 ± 0.01								1.9 ± 0.3				
Burden: Tg	199.6 ± 0.2								191 ± 29				
Stratosphere	34.4 ± 0.1								42				
Troposphere	165.2 ± 0.3		163	155 ± 10	136	172	150	141	149 ± 23	155 ± 10	169	148–153	157.4
IHD (ppbv)	29.4 ± 0.4												
Lifetime (years)	2.1 ± 0.003		1.8	2.1	1.9	2.2	1.4	1.9	1.4 ± 0.2	2	2.2	1.9–2.0	2.1

^{a} Up-scaled from 0.5 to 3 Tg/yr to match literature recommendations (Paulot et al., 2021); ^{b} the dry deposition velocity of H$_2$ Paulot et al. (2021) has been reduced by 6% (from the continental global mean of 0.035 to 0.033 cms^{-1} to improve simulated H$_2$ especially in polar latitudes. VOC = volatile organic compound. IHD = interhemispheric difference.

5 Conclusions

In this study, we have successfully extended and used the EMAC model to undertake simulations of H$_2$ atmospheric dynamics, constrained by flux boundary conditions for both H$_2$ and CH$_4$. Comparing the EMAC model output with observational data at 56 stations from the NOAA GML Carbon Cycle Cooperative Global Air Sampling Network generally indicates very good agreement at global scale. Excellent results are achieved at observational stations free from direct anthropogenic perturbation, suggesting that atmospheric source, sink and transport processes are accurately represented, while model performance is degraded at stations impacted by nearby pollution sources. Our H$_2$ budget is also in good agreement with bottom-up estimates in the literature. We find that the EMAC model simulates the CH$_4$ chemical lifetime in excellent agreement with observational estimates, which suggests the model calculates hydroxyl radical mixing ratios in a representative manner. We conclude

that correctly simulating the oxidising capacity of the atmosphere is a key requirement for high accuracy simulation of H_2 dynamics.

Appendix A: List of observational stations

Table A1. Observational Stations from the NOAA GML Carbon Cycle Cooperative Global Air Sampling Network.

| Station code	Station Name	Latitude	Longitude	Elevation (masl)	Country	Cooperating Agencies
ALT	Alert, Nunavut	82.4508° North	62.5072° West	185	Canada	Environment Canada
AMY	Anmyeon-do	36.5389° North	126.3295° East	47	Republic of Korea	Korea Global Atmosphere Watch Center, Korea Meteorological Administration
ASC	Ascension Island	7.9667° South	14.4° West	85	United Kingdom	Met Office (United Kingdom)
ASK	Assekrem	23.2625° North	5.6322° East	2710	Algeria	Office National de la Meteorologie
AZR	Terceira Island, Azores	38.766° North	27.375° West	19	Portugal	Instituto Nacional de Meteorologia e Geofisica
BHD	Baring Head Station	41.4083° South	174.871° East	85	New Zealand	National Institute of Water and Atmospheric Research
BKT	Bukit Kototabang	0.202° South	100.318° East	845	Indonesia	Bureau of Meteorology and Geophysics
BMW	Tudor Hill, Bermuda	32.2647° North	64.8788° West	30	United Kingdom	Bermuda Institute of Ocean Sciences
BRW	Barrow Atmospheric Baseline Observatory	71.323° North	156.6114° West	11	United States	NOAA Global Monitoring Laboratory
CBA	Cold Bay, Alaska	55.21° North	162.72° West	21.34	United States	U.S. National Weather Service
CGO	Cape Grim, Tasmania	40.683° South	144.69° East	94	Australia	CSIRO
CHR	Christmas Island	1.7° North	157.1518° West	0	Republic of Kiribati	Dive Kiribati
CIB	Centro de Investigacion de la Baja Atmosfera (CIBA)	41.81° North	4.93° West	845	Spain	Centro de Investigacion de la Baja Atmosfera, University of Valladolid
CPT	Cape Point	34.3523° South	18.4891° East	230	South Africa	South African Weather Service
CRZ	Crozet Island	46.4337° South	51.8478° East	197	France	Centre des Faibles Radioactivities/TAAF
DSI	Dongsha Island	20.6992° North	116.7297° East	3	Taiwan	National Central University, Taiwan
EIC	Easter Island	27.1597° South	109.4284° West	47	Chile	Direccion Meteorologica de Chile
GMI	Mariana Islands	13.386° North	144.656° East	0	Guam	University of Guam/Marine Laboratory
HBA	Halley Station, Antarctica	75.55° South	25.63° West	30	United Kingdom	British Antarctic Survey
HPB	Hohenpeissenberg	47.8011° North	11.0245° East	985	Germany	Deutscher Wetterdienst
HUN	Hegyhatsal	46.9559° North	16.6521° East	248	Hungary	Institute for Nuclear Research, Hungarian Academy of Sciences
ICE	Storhofdi, Vestmannaeyjar	63.3998° North	20.2884° West	118	Iceland	Icelandic Meteorological Office
IZO	Izana, Tenerife, Canary Islands	28.309° North	16.499° West	2372.9	Spain	Izana Observatory/Meteorological State Agency of Spain
KEY	Key Biscayne, Florida	25.6654° North	80.158° West	1	United States	NOAA Atlantic Oceanographic and Meteorological Laboratory
KUM	Cape Kumukahi, Hawaii	19.5608° North	154.8883° West	8	United States	NOAA Global Monitoring Laboratory
LLN	Lulin	23.47° North	120.87° East	2862	Taiwan	Lulin Atmospheric Background Station
LMP	Lampedusa	35.5181° North	12.6322° East	45	Italy	Ente per le Nuove tecnologie, l'Energia e l'Ambiente
MEX	High Altitude Global Climate Observation Center	18.9841° North	97.311° West	4464	Mexico	Sistema Internacional de Monitoreo Ambiental
MHD	Mace Head, County Galway	53.326° North	9.899° West	5	Ireland	National University of Ireland, Galway
MID	Sand Island, Midway	28.2186° North	177.3678° West	4.6	United States	U.S. Fish and Wildlife Service
MLO	Mauna Loa, Hawaii	19.5362° North	155.5763° West	3397	United States	NOAA Global Monitoring Laboratory
NAT	Farol De Mae Luiza Lighthouse	5.7952° South	35.1853° West	50	Brazil	Instituto de Pesquisas Energéticas e Nucleares, Il Centrode Química e Meio Ambiente, Divisao de Quimica Ambiental
NMB	Gobabeb	23.58° South	15.03° East	456	Namibia	Gobabeb Training and Research Center
NWR	Niwot Ridge, Colorado	40.0531° North	105.5864° West	3523	United States	University of Colorado/INSTAAR
OXK	Ochsenkopf	50.0301° North	11.8084° East	1022	Germany	Max Planck Institute for Biogeochemistry
PAL	Pallas-Sammaltunturi, GAW Station	67.9733° North	24.1157° East	565	Finland	Finnish Meteorological Institute
PSA	Palmer Station, Antarctica	64.7742° South	64.0527° West	10	United States	National Science Foundation
RPB	Ragged Point	13.165° North	59.432° West	15	Barbados	Private Party
SDZ	Shangdianzi	40.65° North	117.117° East	293	China	Chinese Academy of Meteorological Sciences (CAMS) and Beijing Meteorological Bureau (BMB), China Meteorological Administration (CMA)
SEY	Mahe Island	4.6824° South	55.5325° East	2	Seychelles	Seychelles Bureau of Standards
SGP	Southern Great Plains, Oklahoma	36.607° North	97.489° West	314	United States	Lawrence Berkeley National Laboratory
SHM	Shemya Island, Alaska	52.7112° North	174.126° East	23	United States	Chugach McKinley
SMO	Tutuila	14.2474° South	170.5644° West	42	American Samoa	NOAA Global Monitoring Laboratory
SPO	South Pole, Antarctica	89.98° South	24.8° West	2810	United States	National Science Foundation
SUM	Summit	72.5962° North	38.422° West	3209.54	Greenland	National Science Foundation Office of Polar Programs
SYO	Syowa Station, Antarctica	69.0125° South	39.59° East	14	Japan	National Institute of Polar Research
TAP	Tae-ahn Peninsula	36.7376° North	126.1328° East	16	Republic of Korea	Korea Centre for Atmospheric Environment Research
THD	Trinidad Head, California	41.0541° North	124.151° West	107	United States	Scientific Aviation, Inc, NOAA Global Monitoring Laboratory, AGAGE, Scripps Institution of Oceanography, Humboldt State University Marine Laboratory
TIK	Hydrometeorological Observatory of Tiksi	71.5965° North	128.8887° East	19	Russia	
TPI	Taiping Island	10.3786° North	114.3711° East	4	Taiwan	
USH	Ushuaia	54.8484° South	68.3106° West	12	Argentina	Servicio Meteorologico Nacional
UTA	Wendover, Utah	39.9018° North	113.7181° West	1327	United States	Beth Anderson/ NWS Cooperative Observer
UUM	Ulaan Uul	44.4516° North	111.0956° East	1007	Mongolia	Mongolian Hydrometeorological Research Institute
WIS	Weizmann Institute of Science at the Arava Institute, Ketura	29.9646° North	35.0605° East	151	Israel	Weizmann Institute of Science and Arava Institute for Environmental Studies
WLG	Mt. Waliguan	36.2879° North	100.8964° East	3810	Peoples Republic of China	Chinese Academy of Meteorological Sciences (CAMS) and Qinghai Meteorological Bureau (QMB), China Meteorological Administration (CMA)
ZEP	Ny-Alesund, Svalbard	78.9067° North	11.8883° East	474	Norway and Sweden	Zeppelin Station/University of Stockholm Meteorological Institute

295 **Appendix B: Additional results**
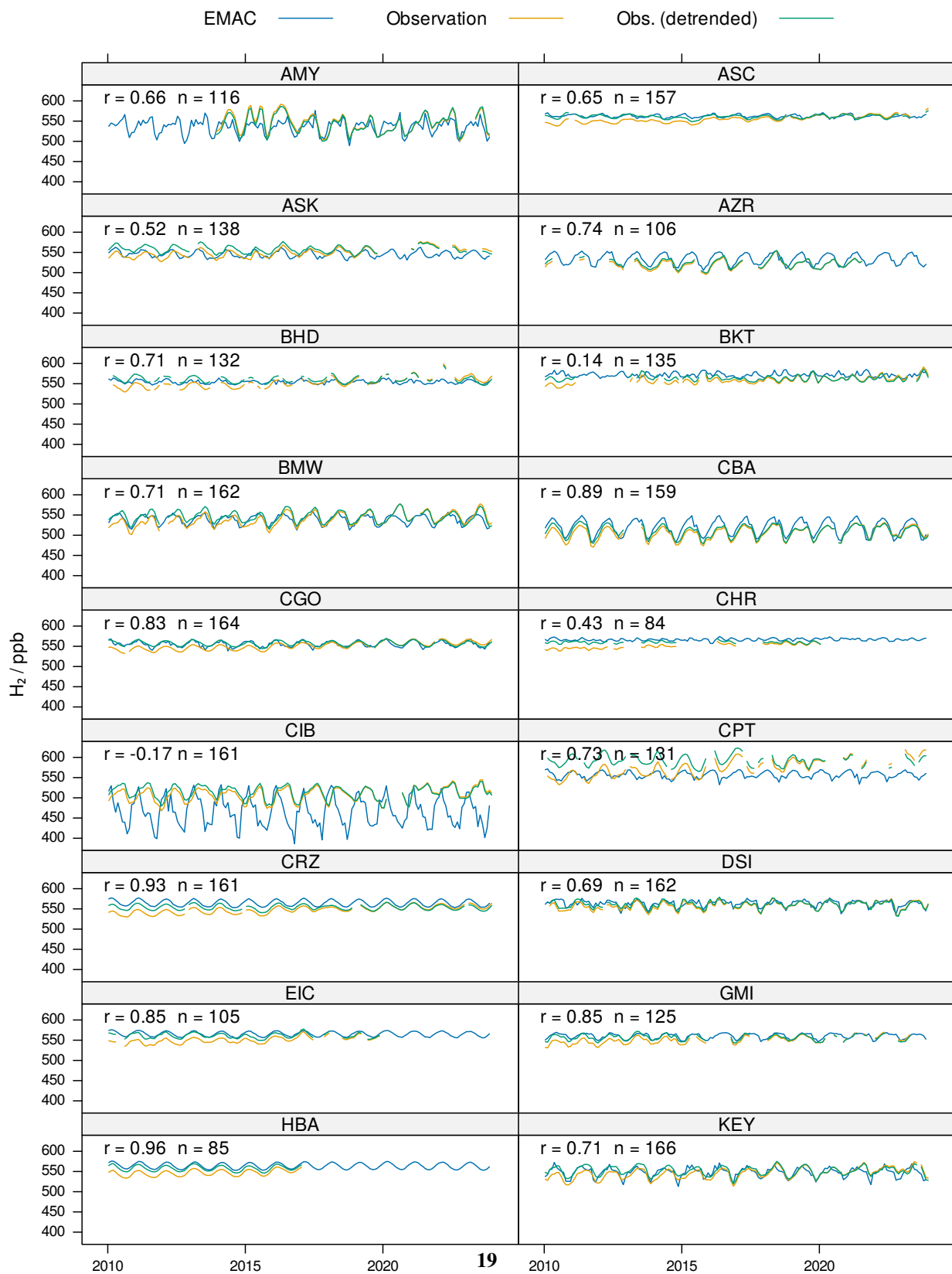
Figure B1. Time series comparison of observational and EMAC model data for H$_2$. [Other stations part 1]
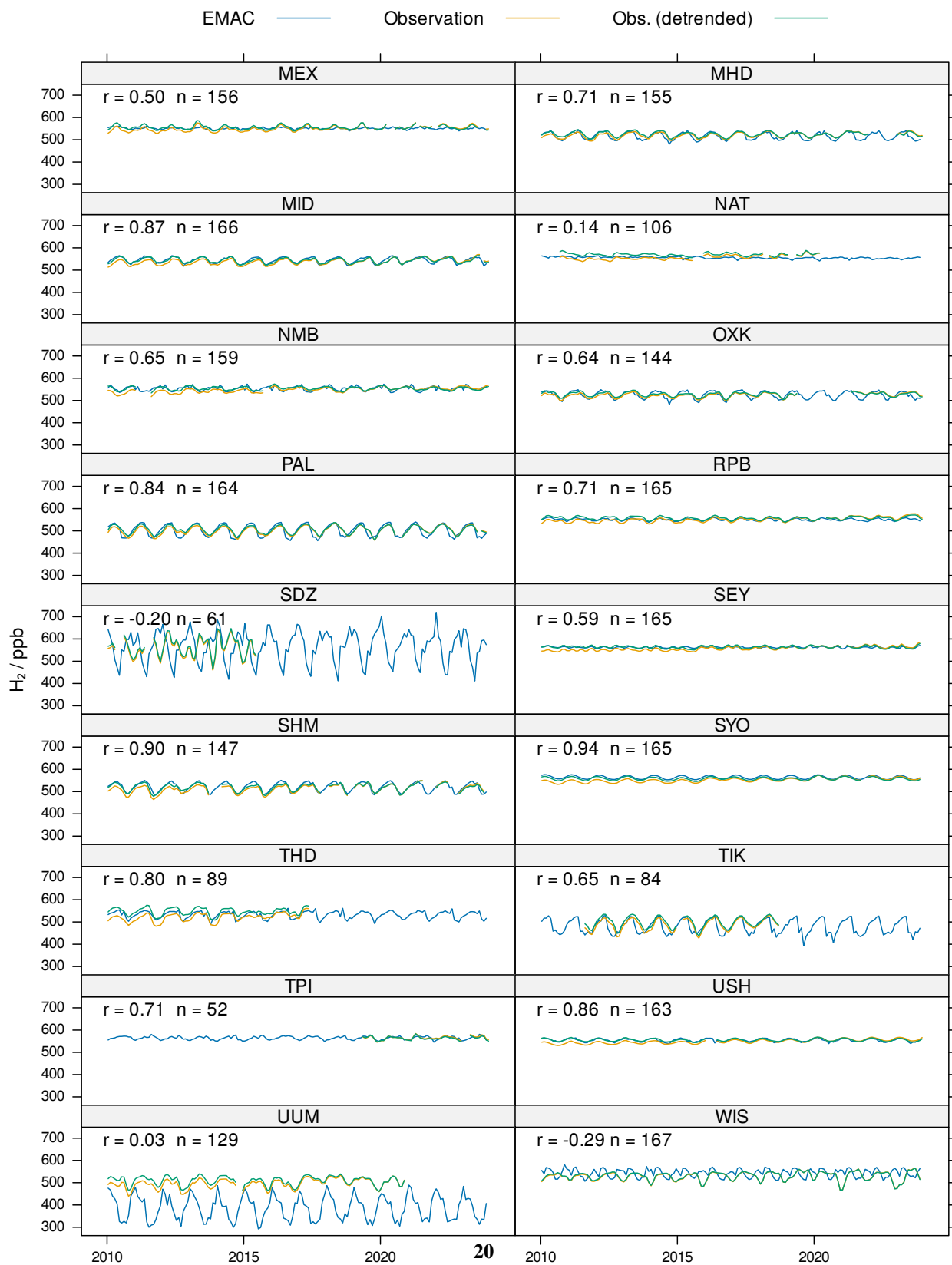
Figure B2. Time series comparison of observational and EMAC model data for H_2. [Other stations part 2]
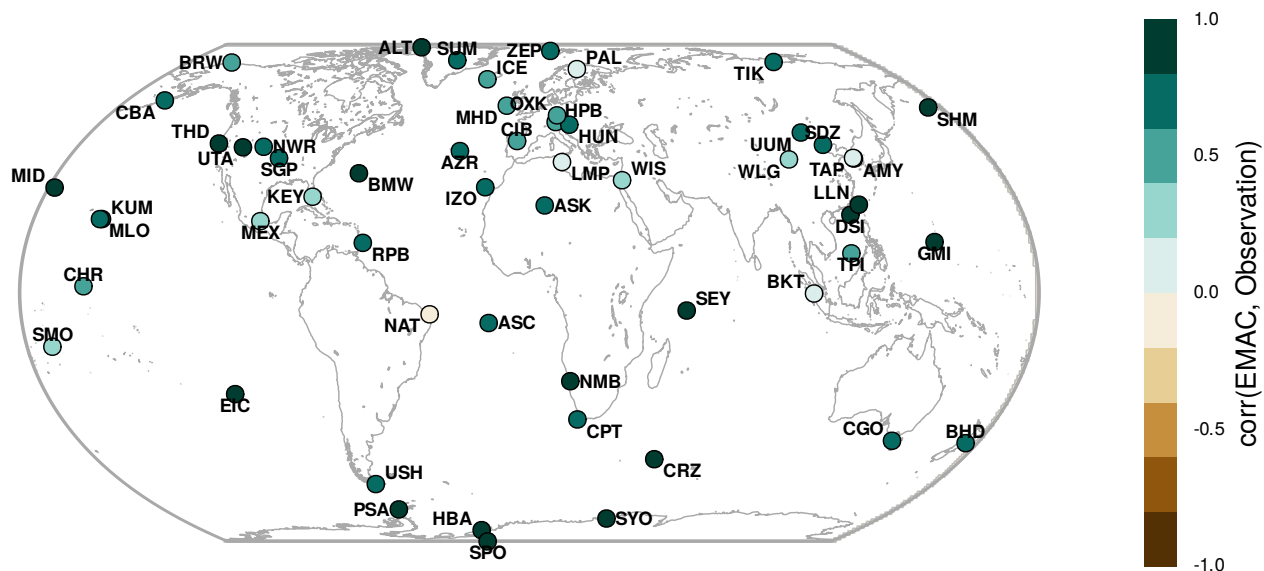
Figure B3. Pearson correlation coefficient between EMAC CH$_4$ mixing ratios and observational data.

Table B1. Comparison of mean model and observational H_2 mixing ratios. Δ = Model $-$ Observed, while r denotes the Pearson correlation coefficient. In the case of the BKT station, the EMAC value of one grid cell to the west of the station is used as it is considered more representative.

Station	Longitude	Latitude	# values	H_2 EMAC (ppb)	H_2 Observed (ppb)	Δ (ppb)	r
ALT	-62.5	82.5	168	504	501	3.16	0.93
AMY	126	36.5	116	536	543	-7.31	0.66
ASC	-14.4	-7.97	158	562	561	1.25	0.65
ASK	5.63	23.3	139	545	558	-13.1	0.52
AZR	-27.4	38.8	106	533	523	10.4	0.74
BHD	175	-41.4	133	554	561	-6.42	0.71
BKT	100	-0.202	136	572	563	8.16	0.14
BMW	-64.9	32.3	163	539	546	-7.05	0.71
BRW	-157	71.3	168	502	507	-4.79	0.81
CBA	-163	55.2	160	520	510	10.0	0.89
CGO	145	-40.7	165	555	557	-1.59	0.83
CHR	-157	1.70	84	567	560	7.01	0.43
CIB	-4.93	41.8	162	467	514	-46.8	-0.17
CPT	18.5	-34.4	131	557	593	-35.8	0.73
CRZ	51.8	-46.4	162	564	554	10.3	0.93
DSI	117	20.7	163	563	560	2.64	0.69
EIC	-109.	-27.2	105	565	561	4.20	0.85
GMI	145	13.4	125	560	557	3.33	0.85
HBA	-26.2	-75.6	85	564	558	5.77	0.96
HPB	11.0	47.8	168	526	527	-1.12	0.56
HUN	16.7	47.0	168	513	523	-9.82	0.39
ICE	-20.3	63.4	168	518	522	-3.95	0.86
IZO	-16.5	28.3	168	545	551	-6.16	0.60
KEY	-80.2	25.7	167	548	552	-3.64	0.71
KUM	-155	19.6	168	544	544	0.158	0.75
LLN	121	23.5	168	563	565	-1.87	0.63
LMP	12.6	35.5	168	517	532	-14.5	0.045
MEX	-97.3	19.0	157	551	556	-5.10	0.50
MHD	-9.90	53.3	156	517	525	-8.05	0.71
MID	-177	28.2	167	544	543	0.816	0.87
MLO	-156	19.5	168	558	548	10.4	0.70
NAT	-35.2	-5.68	106	553	570	-17.0	0.14
NMB	15.0	-23.6	160	554	554	0.144	0.65
NWR	-106	40.1	168	547	536	11.2	0.59
OXK	11.8	50.0	145	525	528	-3.20	0.64
PAL	24.1	68.0	164	503	506	-2.91	0.84
PSA	-64.1	-64.8	168	564	557	6.41	0.95
RPB	-59.4	13.2	166	550	557	-6.93	0.71
SDZ	117	40.6	61	566	569	-2.80	-0.20
SEY	55.5	-4.68	165	563	564	-1.21	0.59
SGP	-97.5	36.6	168	507	519	-12.3	0.77
SHM	174	52.7	147	521	518	2.91	0.90
SMO	-171	-14.2	168	567	561	5.50	0.65
SPO	-24.8	-89.5	168	564	558	5.79	0.96
SUM	-38.4	72.6	168	522	526	-4.01	0.81
SYO	39.6	-69.0	165	564	558	6.03	0.94
TAP	126	36.7	168	535	547	-12.8	0.62
THD	-124	41.1	89	532	547	-15.1	0.80
TIK	129	71.6	84	479	499	-19.9	0.65
TPI	114	10.4	53	564	563	1.53	0.71
USH	-68.3	-54.8	164	554	556	-1.24	0.86
UTA	-114	39.9	168	527	514	12.9	0.82
UUM	111	44.5	129	388	508	-121.	0.034
WIS	35.0	30.3	167	543	530	13.6	-0.29
WLG	101	36.3	168	527	529	-1.28	0.57
ZEP	11.9	78.9	168	515	513	1.85	0.94

300

305

References

Akagi, S. K., Yokelson, R. J., Wiedinmyer, C., Alvarado, M. J., Reid, J. S., Karl, T., Crounse, J. D., and Wennberg, P. O.: Emission factors for open and domestic biomass burning for use in atmospheric models, Atmospheric Chemistry and Physics, 11, 4039–4072, https://doi.org/10.5194/acp-11-4039-2011, 2011.

Andreae, M. O.: Emission of trace gases and aerosols from biomass burning–an updated assessment, Atmospheric Chemistry and Physics, 19, 8523–8546, https://doi.org/10.5194/acp-19-8523-2019, 2019.

Archibald, A. T., Levine, J. G., Abraham, N. L., Cooke, M. C., Edwards, P. M., Heard, D. E., Jenkin, M. E., Karunaharan, A., Pike, R. C., Monks, P. S. Shallcross, D. E., Telford, P. J., Whalley, L. K., and Pyle, J. A.: Impacts of HOx regeneration and recycling in the oxidation of isoprene: Consequences for the composition of past, present and future atmospheres, Geophysical Research Letters, 38, L05 804, https://doi.org/10.1029/2010gl046520, 2011.

Astitha, M., Lelieveld, J., Abdel Kader, M., Pozzer, A., and de Meij, A.: Parameterization of dust emissions in the global atmospheric chemistry-climate model EMAC: impact of nudging and soil properties, Atmospheric Chemistry and Physics, 12, 11 057–11 083, https://doi.org/10.5194/acp-12-11057-2012, 2012.

Bourtsoukidis, E., Pozzer, A., Sattler, T., Matthaios, V. N., Ernle, L., Edtbauer, A., Fischer, H., Könemann, T., Osipov, S., Paris, J.-D., Pfannerstill, E. Y., Stönner, C., Tadic, I., Walter, D., Wang, N., Lelieveld, J., and Williams, J.: The Red Sea Deep Water is a potent source of atmospheric ethane and propane, Nature Communications, 11, 447, https://doi.org/10.1038/s41467-020-14375-0, 2020.

Brasseur, G. P., Kiehl, J. T., Müller, J.-F., Schneider, T., Granier, C., Tie, X. X., and Hauglustaine, D.: Past and future changes in global tropospheric ozone: Impact on radiative forcing, Geophysical Research Letters, 25, 3807–3810, https://doi.org/10.1029/1998gl900013, 1998.

Derwent, R., Simmonds, P., O'Doherty, S., Manning, A., Collins, W., and Stevenson, D.: Global environmental impacts of the hydrogen economy, International Journal of Nuclear Hydrogen Production and Application, 1, 57–67, https://doi.org/10.1504/IJNHPA.2006.009869, 2006.

Derwent, R. G., Stevenson, D. S., Utembe, S. R., Jenkin, M. E., Khan, A. H., and Shallcross, D. E.: Global modelling studies of hydrogen and its isotopomers using STOCHEM-CRI: Likely radiative forcing consequences of a future hydrogen economy, International Journal of Hydrogen Energy, 45, 9211–9221, https://doi.org/10.1016/j.ijhydene.2020.01.125, 2020.

Ehhalt, D. H. and Rohrer, F.: The tropospheric cycle of H_2: a critical review, Tellus B: Chemical and Physical Meteorology, 61B, 500—-535, https://doi.org/10.1111/j.1600-0889.2009.00416.x, 2009.

Ehhalt, D. H. and Rohrer, F.: The dependence of soil H_2 uptake on temperature and moisture: a reanalysis of laboratory data, Tellus B: Chemical and Physical Meteorology, 63B, 1040—-1051, https://doi.org/10.1111/j.1600-0889.2011.00581.x, 2011.

Ehhalt, D. H. and Rohrer, F.: Deposition velocity of H_2: a new algorithm for its dependence on soil moisture and temperature, Tellus B: Chemical and Physical Meteorology, 65, 19 904, https://doi.org/10.3402/tellusb.v65i0.19904, 2013a.

Ehhalt, D. H. and Rohrer, F.: Dry deposition of molecular hydrogen in the presence of H_2 production, Tellus B: Chemical and Physical Meteorology, 65, 20 620, https://doi.org/10.3402/tellusb.v65i0.20620, 2013b.

Ellis, G. S. and Gelman, S. E.: Model predictions of global geologic hydrogen resources, Science Advances, 10, eado0955, https://doi.org/10.1126/sciadv.ado0955, 2024.

Esquivel-Elizondo, S., Hormaza Mejia, A., Sun, T., Shrestha, E., Hamburg, S. P., and Ocko, I. B.: Wide range in estimates of hydrogen emissions from infrastructure, Frontiers in Energy Research, 11, 1207 208, https://doi.org/10.3389/fenrg.2023.1207208, 2023.

345 Fan, Z., Sheerazi, H., Bhardwaj, A., Corbeau, A.-S., Longobardi, K., Castañeda, A., Merz, A.-K., Woodall, C. M., Agrawal, M., Orozco-Sanchez, S., and Friedmann, J.: Hydrogen leakage: a potential risk for the hydrogen economy, The Center on Global Energy Policy at Columbia University, pp. 1-33, https://www.energypolicy.columbia.edu/sites/default/files/file-uploads/HydrogenLeakageRegulations_CGEP_Commentary_063022.pdf (last access: 6 September 2024), 2022.

Galimova, T., Ram, M., and Breyer, C.: Mitigation of air pollution and corresponding impacts during a global energy transition towards
350 100% renewable energy system by 2050, Energy Reports, 8, 14 124–14 143, https://doi.org/10.1016/j.egyr.2022.10.343, 2022.

Ganzeveld, L., Bouwman, L., Stehfest, E., van Vuuren, D. P., Eickhout, B., and Lelieveld, J.: Impact of future land use and land cover changes on atmospheric chemistry-climate interactions, Journal of Geophysical Research: Atmospheres, 115, D23 301, https://doi.org/10.1029/2010jd014041, 2010.

Giglio, L., Randerson, J. T., and van der Werf, G. R.: Analysis of daily, monthly, and annual burned area using the fourth-generation global
355 fire emissions database (GFED4), Journal of Geophysical Research: Biogeosciences, 118, 317–328, https://doi.org/10.1002/jgrg.20042, 2013.

GLDAS: GLDAS Soil Land Surface, https://ldas.gsfc.nasa.gov/gldas/soils, last access: 24 September 2024, 2024.

Granier, C., Darras, S., Denier van der Gon, H., Doubalova, J., Elguindi, N., Galle, B., Gauss, M., Guevara, M., Jalkanen, J.-P., Kuenen, J., Liousse, C., Quack, B., Simpson, D., and Sindelarova, K.: The Copernicus Atmosphere Monitoring Service global and regional emissions
360 (April 2019 version), Copernicus Atmosphere Monitoring Service (CAMS) report, pp. 1–54, https://doi.org/10.24380/d0bn-kx16, 2019.

Guelle, W., Schulz, M., Balkanski, Y., and Dentener, F.: Influence of the source formulation on modeling the atmospheric global distribution of sea salt aerosol, Journal of Geophysical Research: Atmospheres, 106, 27 509–27 524, https://doi.org/10.1029/2001JD900249, 2001.

Guenther, A., Hewitt, C. N., Erickson, D., Fall, R., Geron, C., Graedel, T., Harley, P., Klinger, L., Lerdau, M., McKay, W. A., Pierce, T., Scholes, B., Steinbrecher, R., Tallamraju, R., Taylor, J., and Zimmerman, P.: A global model of natural volatile organic compound
365 emissions, Journal of Geophysical Research: Atmospheres, 100, 8873–8892, https://doi.org/10.1029/94JD02950, 1995.

Hand, E.: Hidden Hydrogen. Does Earth hold vast stores of a renewable carbon-free fuel?, Science, 379, 630–636, https://doi.org/10.1126/science.adh1460, 2023.

Hauglustaine, D. A. and Ehhalt, D. H.: A three-dimensional model of molecular hydrogen in the troposphere, Journal of Geophysical Research: Atmospheres, 107, 4330, https://doi.org/10.1029/2001JD001156, 2002.

370 Hersbach, H., Bell, B., Berrisford, P., Hirahara, S., Horányi, A., Muñoz-Sabater, J., Nicolas, J., Peubey, C., Radu, R., Schepers, D., Simmons, A., Soci, C., Abdalla, S., Abellan, X., Balsamo, G., Bechtold, P., Biavati, G., Bidlot, J., Bonavita, M., De Chiara, G., Dahlgren, P., Dee, D., Diamantakis, M., Dragani, R., Flemming, J., Forbes, R., Fuentes, M., Geer, A., Haimberger, L., Healy, S., Hogan, R. J., Hólm, E., Janisková, M., Keeley, S., Laloyaux, P., Lopez, P., Lupu, C., Radnoti, G., de Rosnay, P., Rozum, I., Vamborg, F., Villaume, S., and Thépaut, J.-N.: The ERA5 global reanalysis, Quarterly Journal of the Royal Meteorological Society, 146, 1999–2049,
375 https://doi.org/10.1002/qj.3803, 2020.

Hersbach, H., Bell, B., Berrisford, P., Biavati, G., Horányi, A., Muñoz Sabater, J., Nicolas, J., Peubey, C., Radu, R., Rozum, I., Schepers, D., Simmons, A., Soci, C., Dee, D., and Thépaut, J.-N.: ERA5 hourly data on single levels from 1940 to present, Copernicus Climate Change Service (C3S) Climate Data Store (CDS) (last access: 19 September 2024), https://doi.org/10.24381/cds.adbb2d47, 2023.

Holmes, C. D., Prather, M. J., Søvde, O. A., and Myhre, G.: Future methane, hydroxyl, and their uncertainties: key climate and emission
380 parameters for future predictions, Atmospheric Chemistry and Physics, 13, 285–302, https://doi.org/10.5194/acp-13-285-2013, 2013.

Houweling, S., Kaminski, T., Dentener, F., Lelieveld, J., and Heimann, M.: Inverse modeling of methane sources and sinks using the adjoint of a global transport model, Journal of Geophysical Research: Atmospheres, 104, 26 137–26 160, https://doi.org/10.1029/1999JD900428, 1999.

Hydrogen Council: Hydrogen for Net-Zero. A critical cost-competitive energy vector, pp. 1-56, https://hydrogencouncil.com/en/hydrogen-for-net-zero/ (last access: 6 September 2024), 2021.

International Energy Agency: Energy Technology Perspectives 2020. Special Report on Carbon Capture Utilisation and Storage: CCUS in clean energy transitions., pp. 1-174, https://www.oecd-ilibrary.org/energy/energy-technology-perspectives-2020-special-report-on-carbon-capture-utilisation-and-storage_208b66f4-en (last access: 6 September 2024), 2020.

International Energy Agency: Global Hydrogen Review 2023, pp. 1-176, https://www.iea.org/reports/global-hydrogen-review-2023 (last access: 6 September 2024), 2023.

Jöckel, P., Tost, H., Pozzer, A., Brühl, C., Buchholz, J., Ganzeveld, L., Hoor, P., Kerkweg, A., Lawrence, M. G., Sander, R., Steil, B., Stiller, G., Tanarhte, M., Taraborrelli, D., van Aardenne, J., and Lelieveld, J.: The atmospheric chemistry general circulation model ECHAM5/MESSy1: consistent simulation of ozone from the surface to the mesosphere, Atmospheric Chemistry and Physics, 6, 5067–5104, https://doi.org/10.5194/acp-6-5067-2006, 2006.

Jöckel, P., Kerkweg, A., Pozzer, A., Sander, R., Tost, H., Riede, H., Baumgaertner, A., Gromov, S., and Kern, B.: Development cycle 2 of the Modular Earth Submodel System (MESSy2), Geoscientific Model Development, 3, 717–752, https://doi.org/10.5194/gmd-3-717-2010, 2010.

Kaiser, J. W., Heil, A., Andreae, M. O., Benedetti, A., Chubarova, N., Jones, L., Morcrette, J.-J., Razinger, M., Schultz, M. G., Suttie, M., and van der Werf, G. R.: Biomass burning emissions estimated with a global fire assimilation system based on observed fire radiative power, Biogeosciences, 9, 527–554, https://doi.org/10.5194/bg-9-527-2012, 2012.

Kerkweg, A., Sander, R., Tost, H., and Jöckel, P.: Technical note: Implementation of prescribed (OFFLEM), calculated (ONLEM), and pseudo-emissions (TNUDGE) of chemical species in the Modular Earth Submodel System (MESSy), Atmospheric Chemistry and Physics, 6, 3603–3609, https://doi.org/10.5194/acp-6-3603-2006, 2006.

Klingmüller, K., Metzger, S., Abdelkader, M., Karydis, V. A., Stenchikov, G. L., Pozzer, A., and Lelieveld, J.: Revised mineral dust emissions in the atmospheric chemistry–climate model EMAC (MESSy 2.52 DU_Astitha1 KKDU2017 patch), Geoscientific Model Development, 11, 989–1008, https://doi.org/10.5194/gmd-11-989-2018, 2018.

Martin, A., Gayler, V., Steil, B., Klingmüller, K., Jöckel, P., Tost, H., Lelieveld, J., and Pozzer, A.: Evaluation of the coupling of EMACv2.55 to the land surface and vegetation model JSBACHv4, Geoscientific Model Development, 17, 5705–5732, https://doi.org/10.5194/gmd-17-5705-2024, 2024.

Millington, R. J. and Quirk, J. P.: Permeability of Porous Media, Nature, 183, 387–388, https://doi.org/10.1038/183387a0, 1959.

Nicely, J. M., Duncan, B. N., Hanisco, T. F., Wolfe, G. M., Salawitch, R. J., Deushi, M., Haslerud, A. S., Jöckel, P., Josse, B., Kinnison, D. E., Klekociuk, A., Manyin, M. E., Marécal, V., Morgenstern, O., Murray, L. T., Myhre, G., Oman, L. D., Pitari, G., Pozzer, A., Quaglia, I., Revell, L. E., Rozanov, E., Stenke, A., Stone, K., Strahan, S., Tilmes, S., Tost, H., Westervelt, D. M., and Zeng, G.: A machine learning examination of hydroxyl radical differences among model simulations for CCMI-1, Atmospheric Chemistry and Physics, 20, 1341–1361, https://doi.org/10.5194/acp-20-1341-2020, 2020.

Novelli, P. C., Lang, P. M., Masarie, K. A., Hurst, D. F., Myers, R., and Elkins, J. W.: Molecular hydrogen in the troposphere: Global distribution and budget, Journal of Geophysical Research: Atmospheres, 104, 30 427–30 444, https://doi.org/10.1029/1999JD900788, 1999.

Ocko, I. B. and Hamburg, S. P.: Climate consequences of hydrogen emissions, Atmospheric Chemistry and Physics, 22, 9349–9368, https://doi.org/10.5194/acp-22-9349-2022, 2022.

Paulot, F., Paynter, D., Naik, V., Malyshev, S., Menzel, R., and Horowitz, L. W.: Global modeling of hydrogen using GFDL-AM4.1: Sensitivity of soil removal and radiative forcing, International Journal of Hydrogen Energy, 46, 13 446–13 460, https://doi.org/10.1016/j.ijhydene.2021.01.088, 2021.

Paulot, F., Pétron, G., Crotwell, A. M., and Bertagni, M. B.: Reanalysis of NOAA H_2 observations: implications for the H_2 budget, Atmospheric Chemistry and Physics, 24, 4217–4229, https://doi.org/10.5194/acp-24-4217-2024, 2024.

Petron, G., Crotwell, A. M., Madronich, M., Moglia, E., Baugh, K. E., Kitzis, D., Mefford, T., DeVogel, S., Neff, D., Lan, X., Crotwell, M. J., Thoning, K., Wolter, S., and Mund, J. W.: Atmospheric Hydrogen Dry Air Mole Fractions from the NOAA GML Carbon Cycle Cooperative Global Air Sampling Network, 2009–2023 Version: 2024-07-30, https://doi.org/10.15138/WP0W-EZ08, 2024.

Pieterse, G., Krol, M. C., Batenburg, A. M., Steele, L. P., Krummel, P. B., Langenfelds, R. L., and Röckmann, T.: Global modelling of H_2 mixing ratios and isotopic compositions with the TM5 model, Atmospheric Chemistry and Physics, 11, 7001–7026, https://doi.org/10.5194/acp-11-7001-2011, 2011.

Pöschl, U., von Kuhlmann, R., Poisson, N., and Crutzen, P. J.: Development and intercomparison of condensed isoprene oxidation mechanisms for global atmospheric modeling, Journal of Atmospheric Chemistry, 37, 29–52, https://doi.org/10.1023/A:1006391009798, 2000.

Prather, M. J. and Zhu, L.: Resetting tropospheric OH and CH_4 lifetime with ultraviolet H_2O absorption, Science, 385, 201–204, https://doi.org/10.1126/science.adn0415, 2024.

Price, H., Jaeglé, L., Rice, A., Quay, P., Novelli, P. C., and Gammon, R.: Global budget of molecular hydrogen and its deuterium content: Constraints from ground station, cruise, and aircraft observations, Journal of Geophysical Research: Atmospheres, 112, D22 108, https://doi.org/10.1029/2006JD008152, 2007.

Randerson, J. T., van der Werf, G. R., Giglio, L., Collatz, G. J., and Kasibhatla, P. S.: Global fire emissions database, version 4.1 (GFEDv4), ORNL DAAC, Oak Ridge, Tennessee, USA. https://daac.ornl.gov/cgi-bin/dsviewer.pl?ds_id=1293 (last access: 22 December 2024), https://doi.org/10.3334/ORNLDAAC/1293, 2017.

Reifenberg, S. F., Martin, A., Kohl, M., Bacer, S., Hamryszczak, Z., Tadic, I., Röder, L., Crowley, D. J., Fischer, H., Kaiser, K., Schneider, J., Dörich, R., Crowley, J. N., Tomsche, L., Marsing, A., Voigt, C., Zahn, A., Pöhlker, C., Holanda, B. A., Krüger, O., Pöschl, U., Pöhlker, M., Jöckel, P., Dorf, M., Schumann, U., Williams, J., Bohn, B., Curtius, J., Harder, H., Schlager, H., Lelieveld, J., and Pozzer, A.: Numerical simulation of the impact of COVID-19 lockdown on tropospheric composition and aerosol radiative forcing in Europe, Atmospheric Chemistry and Physics, 22, 10 901–10 917, https://doi.org/10.5194/acp-22-10901-2022, 2022.

Rhee, T. S., Brenninkmeijer, C. A. M., Braß, M., and Brühl, C.: Isotopic composition of H_2 from CH_4 oxidation in the stratosphere and the troposphere, Journal of Geophysical Research: Atmospheres, 111, D23 303, https://doi.org/10.1029/2005JD006760, 2006.

Rodell, M., Houser, P. R., Jambor, U., Gottschalck, J., Mitchell, K., Meng, C.-J., Arsenault, K., Cosgrove, B., Radakovich, J., Bosilovich, M., Entin, J. K., Walker, J. P., Lohmann, D., and Toll, D.: The Global Land Data Assimilation System, Bulletin of the American Meteorological Society, 85, 381–394, https://doi.org/10.1175/BAMS-85-3-381, 2004.

Roeckner, E., Bäuml, G., Bonaventura, L., Brokopf, R., Esch, M., Giorgetta, M., Hagemann, S., Kirchner, I., Kornblueh, L., Manzini, E., Rhodin, A., Schlese, U., Schulzweida, U., and Tompkins, A.: Report No 349: the atmospheric general circulation model ECHAM5, Part I., pp. 1–133, https://pure.mpg.de/pubman/faces/ViewItemOverviewPage.jsp?itemId=item_995269 (last access: 22 December 2024), 2003.

455   Roeckner, E., Brokopf, R., Esch, M., Giorgetta, M., Hagemann, S., Kornblueh, L., Manzini, E., Schlese, U., and Schulzweida, U.: Report No. 354: the atmospheric general circulation model ECHAM5, Part II., pp. 1–64, https://pure.mpg.de/pubman/faces/ViewItemOverviewPage.jsp?itemId=item_995221 (last access: 22 December 2024), 2004.

Roeckner, E., Brokopf, R., Esch, M., Giorgetta, M., Hagemann, S., Kornblueh, L., Manzini, E., Schlese, U., and Schulzweida, U.: Sensitivity of Simulated Climate to Horizontal and Vertical Resolution in the ECHAM5 Atmosphere Model, Journal of Climate, 19, 3771–3791,

460   https://doi.org/10.1175/JCLI3824.1, 2006.

Sand, M., Skeie, R. B., Sandstad, M., Krishnan, S., Myhre, G., Bryant, H., Derwent, R., Hauglustaine, D., Paulot, F., Prather, M., and Stevenson, D.: A multi-model assessment of the Global Warming Potential of hydrogen, Communications Earth & Environment, 4, 203, https://doi.org/10.1038/s43247-023-00857-8, 2023.

Sanderson, M. G., Collins, W. J., Derwent, R. G., and Johnson, C. E.: Simulation of Global Hydrogen Levels Using a Lagrangian Three-

465   Dimensional Model, Journal of Atmospheric Chemistry, 46, 15–28, https://doi.org/10.1023/A:1024824223232, 2003.

Schultz, M. G., Diehl, T., Brasseur, G. P., and Zittel, W.: Air pollution and climate-forcing impacts of a global hydrogen economy, Science, 302, 624–627, https://doi.org/10.1126/science.1089527, 2003.

Schultz, M. G., Heil, A., Hoelzemann, J. J., Spessa, A., Thonicke, K., Goldammer, J. G., Held, A. C., Pereira, J. M., and van het Bolscher, M.: Global wildland fire emissions from 1960 to 2000, Global Biogeochemical Cycles, 22, GB2002, https://doi.org/10.1029/2007GB003031,

470   2008.

Seiler, W. and Conrad, R.: Dickinson, R. E. (editor). Contribution of tropical ecosystems to the global budgets of trace gases, especially CH_4, H_2, CO, and N_2O, in: The Geophysiology of Amazonia: Vegetation and Climate Interactions, pp. 133–162, John Wiley, New York, ISBN 0471845116, 1987.

Smith-Downey, N. V., Randerson, J. T., and Eiler, J. M.: Temperature and moisture dependence of soil H_2 uptake measured in the laboratory,

475   Geophysical Research Letters, 33, L14 813, https://doi.org/10.1029/2006GL026749, 2006.

The MESSy Consortium: The Modular Earth Submodel System Version 2.55.2_no-branch_b4754874_H2, https://doi.org/https://doi.org/10.5281/zenodo.15211346, 2025.

Tromp, T. K., Shia, R.-L., Allen, M., Eiler, J. M., and Yung, Y. L.: Potential environmental impact of a hydrogen economy on the stratosphere, Science, 300, 1740–1742, https://doi.org/10.1126/science.1085169, 2003.

480   Truche, L., Donzé, F.-V., Goskolli, E., Muceku, B., Loisy, C., Monnin, C., Dutoit, H., and Cerepi, A.: A deep reservoir for hydrogen drives intense degassing in the Bulqizë ophiolite, Science, 383, 618–621, https://doi.org/10.1126/science.adk9099, 2024.

Van Aardenne, J. A., Dentener, F. J., Olivier, J. G. J., Peters, J. A. H. W., and Ganzeveld, L. N.: The EDGAR 3.2 Fast track 2000 dataset (32FT2000), https://www.researchgate.net/profile/Frank-Dentener/publication/233894132_The_EDGAR_32_Fast_track_2000_dataset_32FT2000/links/02e7e52fa254d80ba0000000/The-

485   EDGAR-32-Fast-track-2000-dataset-32FT2000.pdf (last access: 22 December 2024), 32, 2005.

Warneck, P.: Chemistry of the Natural Atmosphere., International Geophysics Series, Volume 41, pp. 1-757, Academic Press, San Diego, ISBN 9780080954684, 1988.

Warwick, N., Griffiths, P., Keeble, J., Archibald, A., Pyle, J., and Shine, K.: Atmospheric implications of increased Hydrogen use, University of Cambridge and University of Reading, pp. 1-75,

490   https://assets.publishing.service.gov.uk/media/624eca7fe90e0729f4400b99/atmospheric-implications-of-increased-hydrogen-use.pdf (last access: 22 December 2024), 2022.

Warwick, N. J., Bekki, S., Nisbet, E. G., and Pyle, J. A.: Impact of a hydrogen economy on the stratosphere and troposphere studied in a 2-D model, Geophysical Research Letters, 31, L05 107, https://doi.org/10.1029/2003GL019224, 2004.

Warwick, N. J., Archibald, A. T., Griffiths, P. T., Keeble, J., O'Connor, F. M., Pyle, J. A., and Shine, K. P.: Atmospheric composition and climate impacts of a future hydrogen economy, Atmospheric Chemistry and Physics, 23, 13 451–13 467, https://doi.org/10.5194/acp-23-13451-2023, 2023.

Xiao, X., Prinn, R. G., Simmonds, P. G., Steele, L. P., Novelli, P. C., Huang, J., Langenfelds, R. L., O'Doherty, S., Krummel, P. B., Fraser, P. J., Porter, L. W., Weiss, R. F., Salameh, P., and Wang, R. H. J.: Optimal estimation of the soil uptake rate of molecular hydrogen from the Advanced Global Atmospheric Gases Experiment and other measurements, Journal of Geophysical Research: Atmospheres, 112, D07 303, https://doi.org/10.1029/2006JD007241, 2007.

Yang, L. H., Jacob, D. J., Lin, H., Dang, R., Bates, K. H., East, J. D., Travis, K. R., Pendergrass, D. C., and Murray, L. T.: Model underestimates of OH reactivity cause overestimate of hydrogen's climate impact, arXiv pre print, https://arxiv.org/pdf/2408.05127, (last access: 23 December 2024), 2024.

Yashiro, H., Sudo, K., Yonemura, S., and Takigawa, M.: The impact of soil uptake on the global distribution of molecular hydrogen: chemical transport model simulation, Atmospheric Chemistry and Physics, 11, 6701–6719, https://doi.org/10.5194/acp-11-6701-2011, 2011.

Yonemura, S., Yokozawa, M., Kawashima, S., and Tsuruta, H.: Model analysis of the influence of gas diffusivity in soil on CO and H2 uptake, Tellus B: Chemical and Physical Meteorology, 52B, 919–933, https://doi.org/10.3402/tellusb.v52i3.17075, 2000.

Zimmermann, P. H., Brenninkmeijer, C. A. M., Pozzer, A., Jöckel, P., Winterstein, F., Zahn, A., Houweling, S., and Lelieveld, J.: Model simulations of atmospheric methane (1997–2016) and their evaluation using NOAA and AGAGE surface and IAGOS-CARIBIC aircraft observations, Atmospheric Chemistry and Physics, 20, 5787–5809, https://doi.org/10.5194/acp-20-5787-2020, 2020.